THE JOURNAL OF PHYSICAL CHEMISTRY C

Article

pubs.acs.org/JPCC

$TiSi_2O_x$ Coated N-Doped Carbon Nanotubes as Pt Catalyst Support for the Oxygen Reduction Reaction in PEMFCs

Mohammad Norouzi Banis,[†] Shuhui Sun,[†] Xiangbo Meng,[†] Yong Zhang,[†] Zhiqiang Wang,[§] Ruying Li,[†] Mei Cai,[‡] Tsun-Kong Sham,[§] and Xueliang Sun*[,†]

[†]Department of Mechanical and Materials Engineering, The University of Western Ontario, London, Ontario N6A 5B9, Canada

[‡]General Motors R&D Center, Warren, Michigan 48090-9055, United States

[§]Department of Chemistry, University of Western Ontario, London, Ontario N6A 5B7, Canada

Supporting Information

ABSTRACT: Composite nanostrucutres of $TiSi_2O_x$ coated nitrogen-doped carbon nanotubes (NCNTs) were synthesized by a combination of chemical vapor deposition (CVD) and magnetron sputtering processes. The synthesized nanostructures were used as supports for Pt catalyst for oxygen reduction reaction (ORR) in proton exchange memberane fuel cells (PEMFCs). An amorphous layer of $TiSi_2O_x$ with controlled thicknesses was sputtered on NCNTs and followed by post-treatment at high temperature (1000 °C, *An*-$TiSi_2O_x$-NCNTs), inducing TiO_2 nanoparticles of around 5 nm in diameter embedded in the amorphous layer. Further analyses via X-ray absorption spectroscopy of the Ti K edge and Si K edge revealed the Ti atoms were in a TiO_2 rutile environment and the Si atoms were in a SiO_2 environment. Pt nanoparticles with an average diameter of 3 nm were deposited on the composite support, and their electrochemical behaviors toward ORR were studied. It was revealed that, even with lower electrochemical surface area (ECSA), Pt/*An*-$TiSi_2O_x$-NCNTs showed better catalytic activity toward ORR than Pt/NCNT catalysts. The origin of enhanced activity of Pt/*An*-$TiSi_2O_x$-NCNTs was examined by high resolution transmission electron microscopy (HRTEM) and the X-ray absorption near edge structure spectra (XANES) of the deposited Pt nanoparticles.

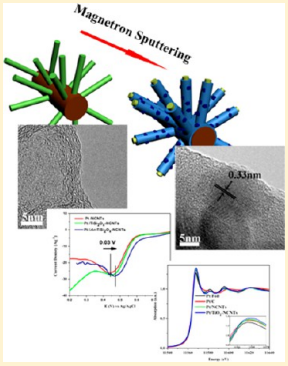

INTRODUCTION

Proton exchange membrane fuel cells (PEMFCs) are considered as one of the most promising energy conversion systems, due to their low emissions and high efficiency for automotive, portable, and stationery applications. To succeed in widespread commercialization, however, the high cost and low durability issues have to be addressed, which are generally associated with electrocatalyst and their support. The most commonly used electrocatalysts in the state of the art PEMFCs are Pt-based nanoparticles supported by high surface area carbon material, accounting for 30−45% of the total cost.[1] Therefore, it is highly desirable to explore electrocatalysts with lower Pt content and enhanced catalytic activity.

One of the main approaches is to develop new catalyst supports that could improve the catalytic activity of electrocatalysts, which can play a key role in enhancing the performance of a PEM fuel cell.[2] In recent years, intensive research has been focused on synthesizing various catalyst supports including nanostructured carbon material,[3−10] metal oxides,[11,12] carbides,[13] and composite structures.[14,15] As an example, carbon nanotubes (CNTs) and nitrogen-doped carbon nanotubes (NCNTs) have been studied extensively due to their unique structures and excellent electrical properties. Many studies have shown that CNTs and NCNT supported Pt catalysts[3,6] exhibit enhanced performance for oxygen reduction reaction (ORR) relative to commercial Pt/C. The past studies suggested that the electrocatalytic activity of Pt clusters can be boosted by the interaction between Pt and the doping atoms of a support (e.g., nitrogen), due to the charge transfer between Pt and these atoms affecting the catalytic activity. In addition, the use of CNTs and NCNTs increases the Pt dispersion, leading to higher Pt utilization.[3,4] Other than carbon based support, studies have been carried out on metal based nanostructures. In most cases, metal oxides and ceramic materials are electrochemically stable in a fuel cell environment, and can act as cocatalysts through affecting the electronic structure of the catalyst.[11,12] Among metal oxides studied for catalyst supports in low temperature fuel cells, titanium oxides (TiO_2) were extensively studied in the form of micro/nanoparticles, nanotubes, and nanowires. Studies have shown that TiO_2 can be an interesting candidate support material, since it has high stability in the fuel cell environment at potentials relevant to the PEMFC cathode.[14] Kang et al. investigated the ORR activity of PtCo on titanium oxide nanotube. Their results showed significant enhancement for ORR and methanol oxidation.[16] The drawback with ceramic material is their weak physical interaction with catalyst

Received: December 3, 2012
Revised: May 1, 2013
Published: June 17, 2013

 © 2013 American Chemical Society dx.doi.org/10.1021/jp3118874 | *J. Phys. Chem. C* 2013, 117, 15457−15467

nanoparticles compared to carbon-based supports, leading to the low dispersion of the catalysts and lower catalytic activity.

To combine the advantages of both carbon and ceramic based supports for low temperature fuel cells, their composite materials were proposed as new supports.[15] Composite catalyst support materials such as titanium oxide modified carbon nanostructures have been reported to have improved the catalytic activity of the electrocatalyst. Beak et al.[17] have shown that the dispersion of Pt nanoparticles using TiO_2 nanoparticles modified carbon support can be improved. It was also found that the interaction between Pt and Ti species had an impact on the electronic state of Pt, contributing to the enhanced ORR activity of Pt. SiO_2 modified carbon nitride has also been studied by Wang et al.,[18] as an electrocatalyst for ORR. They showed that Pt nanoparticles deposited on SiO_2 modified carbon nitride showed a much higher mass activity compared to carbon and carbon nitride supports. This was attributed to the synergistic effect that existed in Pt, carbon nitride, and SiO_2.

To understand the effect of the catalyst supports on the activity of the electrocatalysts for ORR and to design more efficient systems, studies have been focused on several important factors. It has been shown that nitrogen content in NCNTs influences the ORR activity of electrocatalysts.[2,6] Studies have also shown strong metal support interaction (SMSI) between the catalyst supports and Pt nanoparticles plays a key part in the performance of the electrocatalyst.[17] X-ray absorption spectroscopy (XAS) of Pt $L_{2,3}$ and Pt $M_{2,3}$ edges of supported Pt nanoparticles provides a good tool of probing the electronic structure of Pt nanoparticles and understanding the effects of catalyst supports.[19−21] This is directly related to the interaction between the catalysts and their supports.[19,20] Furthermore it has been reported that the morphology and shape of Pt nanostructures influences the ORR activity of the electrocatalyst.[22,23] The Pt nanostructure morphology in turn is closely related to the deposition process and the substrate.

Herein we report the synthesis of a $TiSi_2O_x$-NCNTs hybrid composite directly on carbon paper via chemical vapor deposition (CVD) and magnetron sputtering. The electrocatalytic properties of Pt catalyst supported on $TiSi_2O_x$-NCNTs and *An*-$TiSi_2O_x$-NCNTs on carbon paper for ORR in PEMFCs have been studied. To elucidate the influencing parameters on the ORR activity of the composite nanostructured electrocatalysts, the morphology, physical, and chemical structure of the catalyst supports and Pt nanoparticles were studied. X-ray absorption spectroscopy was used to study the chemical state of Ti and Si atoms in sputtered $TiSi_2O_x$ and the effect of heat treatment. The chemical and electronic structure of Pt nanostructures deposited on the composite catalyst supports were investigated by qualitative and quantitative analysis of X-ray absorption near edge structure spectra of the Pt $L_{2,3}$ edges.

EXPERIMENTAL PROCEDURE

Synthesis. $TiSi_2O_x$-NCNT nanostructures were synthesized by combining CVD and magnetron sputtering processes. In this method, NCNTs were synthesized directly on carbon paper via the CVD method using Fe as the catalyst and melamine (Aldrich, 99%, $C_3H_6N_6$) as the source of carbon and nitrogen.[24−26] In detail, an aluminum (Al) layer with a thickness of 30 nm was sputtered on carbon paper as a buffer layer. On top of this layer, a 1−2 nm thick Fe layer was sputtered to act as the catalyst for NCNT growth. The substrate was placed in the center of a quartz tube. Melamine was put at the low temperature region of the quartz tube (upstream). The tube was mounted on a horizontal electric furnace, and Ar (99.999%) was introduced into the system for 30 min to purge out the air. The temperature was then raised to 800 °C, and held at this temperature for 30 min under a constant flow of Ar (300 sccm). After the system was cooled down to room temperature, the substrate was found being covered by a dark black layer of NCNTs.

The NCNTs on carbon paper provided an open structure suitable for magnetron sputter coating. The substrates were placed in a plasma enhanced chemical vapor deposition-sputtering system (PECVD). A 100 nm layer of $TiSi_2O_x$ was deposited on the NCNTs from a $TiSi_2$ target (Kurt J. Lesker, 2 in., 99.9%) using a RF magnetron (150 W, 10 min) at a working pressure of 1.5×10^{-3} Torr. The oxygen was introduced from the residual oxygen in the sputtering chamber.

The composite nanostructures synthesized on carbon paper were then heat treated in a vacuum oven, resulting in *An*-$TiSi_2O_x$-NCNTs for further studies (*An*: annealed). The nanostructures were positioned in a quartz tube and placed on a horizontal electric furnace. The pressure of the system was lowered down to around 1 mbar before Ar was introduced into the system at a high flow rate to flush out the air. This process was repeated several times. The system was then heated up to 1000 °C at a rate of 10 °C/min and kept at that temperature for 6 h under a chamber pressure of 5 mbar in an Ar (99.999%) environment. After the heat treatment, the color of the samples turned from dark black to dark gray.

Physical Characterization. The morphologies of the products were characterized using a field emission scanning electron microscope (SEM, Hitachi S4800, operated at 5.0 kV) equipped with an energy dispersive X-ray spectroscope (EDX), transmission electron microscope (TEM, Hitachi 7000, operated at 100 kV), and high resolution TEM (HRTEM, JEOL 2010, operated at 200 kV) along with selected area electron diffraction (SAED) pattern. The crystal structure and composition of the products were characterized by X-ray diffractrometer (XRD) using Co $K\alpha_1$ (λ = 0.179 nm) radiation operated at 45 kV and 35 mA. Raman spectroscopy (HORIBA Scientific LabRAM HR) was carried out to provide detailed information on the composite structures.

X-ray Absorption Spectroscopy. The Si K edge and Ti K edge X-ray absorption near edge structure (XANES) measurements were obtained using the soft X-ray microcharacterization beamline (SXRMB; 06B1-1) at the Canadian Light Source (CLS).[27] The Si K edge spectra were collected using an InSb(111) crystal monochromator, and the Ti K edge spectra were collected using a Si(111) crystal monochromator in total electron yield (TEY). The spectra were calibrated using Si and Ti reference samples.

XANES measurements of Pt L_2 edge and Pt L_3 edge were conducted on the 06ID superconducting wiggler sourced hard X-ray microanalysis (HXMA) beamline at the Canadian Light Source and the PNC-XSD (Pacific Northwest Consortium X-ray Science Division) ID-20B beamline of the Advanced Photon Source (APS) at Argonne National Laboratory. The spectra were collected in fluorescence yield using a solid state detector, and the spectra of high purity metal Pt foil were collected in transmission mode for comparison and mono energy calibration.

Pt Deposition. Pt nanoparticles were deposited on $TiSi_2O_x$-NCNT composite nanostructures grown on carbon paper substrate by a formic acid method.[28,29] In this method, the Pt precursor ($H_2PtCl_6{\cdot}6H_2O$, Aldrich, 99.95%) and formic acid

dx.doi.org/10.1021/jp3118874 | J. Phys. Chem. C 2013, 117, 15457−15467

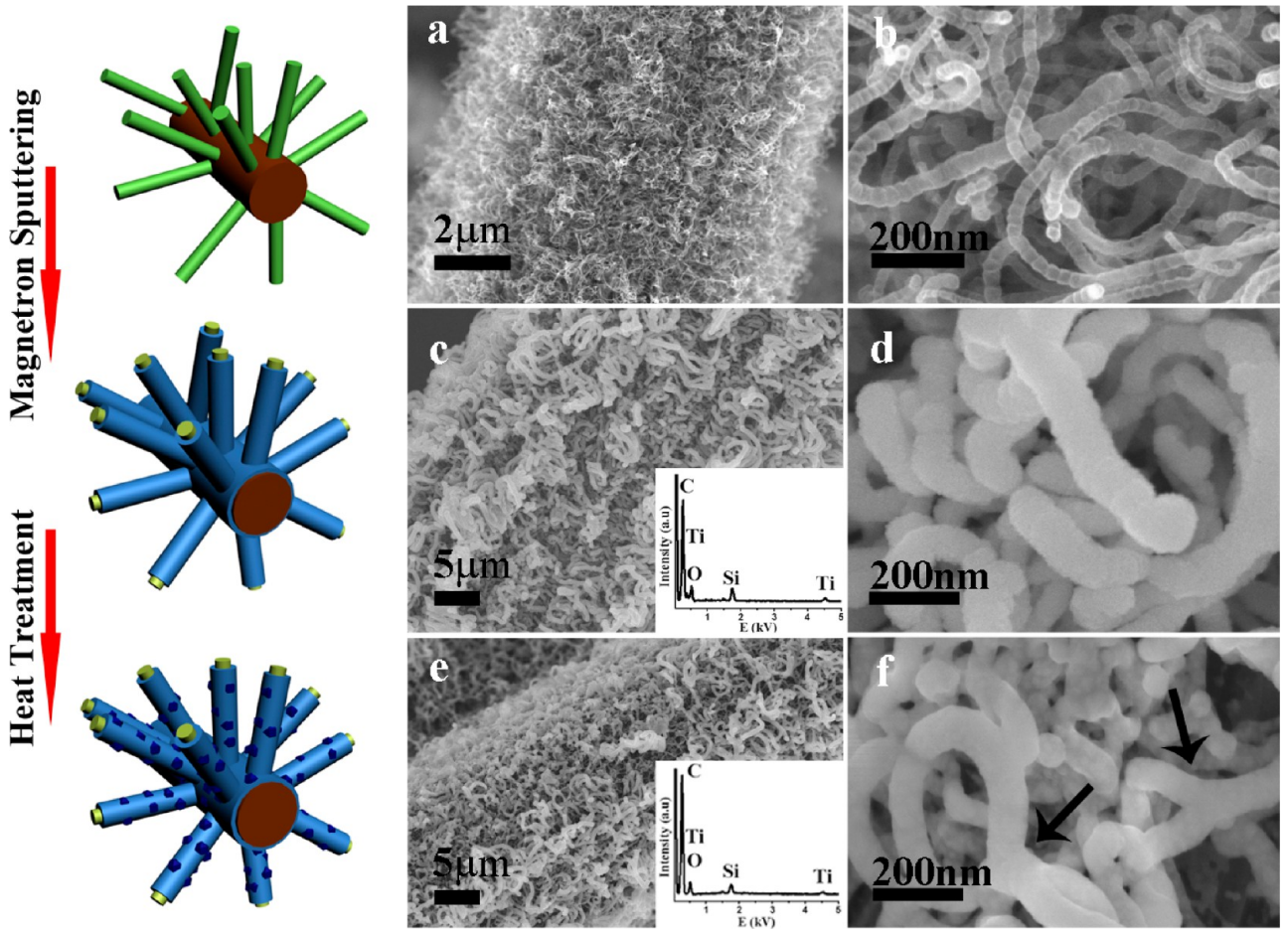

Figure 1. Schematic diagram and SEM images of nanostructures deposited on carbon paper: (a, b) NCNTs; (c, d) $TiSi_2Ox$-NCNTs; (e, f) *An*-$TiSi_2O_x$-NCNTs.

(HCOOH, Aldrich, 98%) were used as received. The synthesis was conducted in deionized water following this reaction:

$$H_2PtCl_6 + 2HCOOH = Pt + 6H^+ + 6Cl^- + 2CO_2(g)$$

In this process, 1 mL of 0.03 M $H_2PtCl_6{\cdot}6H_2O$ and 1 mL of HCOOH were simultaneously mixed with 20 mL of water at room temperature. $TiSi_2O_x$-NCNT nanostructures on carbon paper were immersed in the solution, and the reaction was carried out at 80 °C for ~15 min. In this period, the color of the solution turned from golden orange to dark brown, indicating the formation of Pt nanoparticles. After the solution was cooled down, the composite nanostructures on carbon paper were removed from the solution, washed by deionized water, and dried at room temperature overnight.

Electrochemical Characterization. Pt/composite supports directly grown on carbon paper were used as the working electrode. The carbon paper acted as a support and a current collector. Cyclic voltammetry was conducted at room temperature using an Autolab potentiostat/galvanostat (model PGSTAT-30, Ecochemie, Brinkman Instrument) with a standard three-electrode, two-compartment configuration. Pt wire and Ag/AgCl (3 M NaCl) electrode were used as the counter and reference electrodes, respectively. For hydrogen electrosorption curve measurement, the potential was cycled between −0.159 and 0.991 V at 50 mV s^{-1} to obtain the voltammograms of hydrogen adsorption in Ar-purged 0.5 M H_2SO_4 aqueous solution. For ORR measurement, O_2 (99.99%) was first purged into solution at a position close to the working electrode for at least 30 min. The measurements were conducted by linear potential sweeping from 0.8 to 0.2 V.

For comparison purposes, Pt nanoparticles deposited (via the same synthetic method as above) on NCNTs were also evaluated. The Pt loading in Pt/composite support/carbon paper electrocatalysts was determined by inductively coupled plasma optical emission spectroscopy (ICP-OES).

RESULTS AND DISCUSSION

The morphologies of NCNTs, $TiSi_2O_x$-NCNTs, and *An*-$TiSi_2O_x$-NCNTs are shown in Figure 1. The NCNTs used as the substrates for the composite support define the ultimate morphology of the composite and are a key factor in determining the uniformity of the coated layer. In the CVD method, a thin Fe catalyst layer ensures a good control on the diameter and density of the synthesized NCNTs, as shown in Figure 1a and b.[24,30,31] The NCNTs, as previously reported,[24,32] exhibit typical bamboo-like structures and have a narrow range of diameter between 25 and 50 nm. Furthermore, the unique texture of carbon paper used as a substrate enhances the formation of the 3D open structure of NCNTs with no preferential alignment.[3,26]

SEM images of $TiSi_2O_x$-NCNTs are shown in Figure 1c and d. As seen in these figures, the general morphology of nanostructures on carbon paper is not affected in the sputter coating process, and the $TiSi_2O_x$-NCNTs maintain their 3D

dx.doi.org/10.1021/jp3118874 | J. Phys. Chem. C 2013, 117, 15457−15467

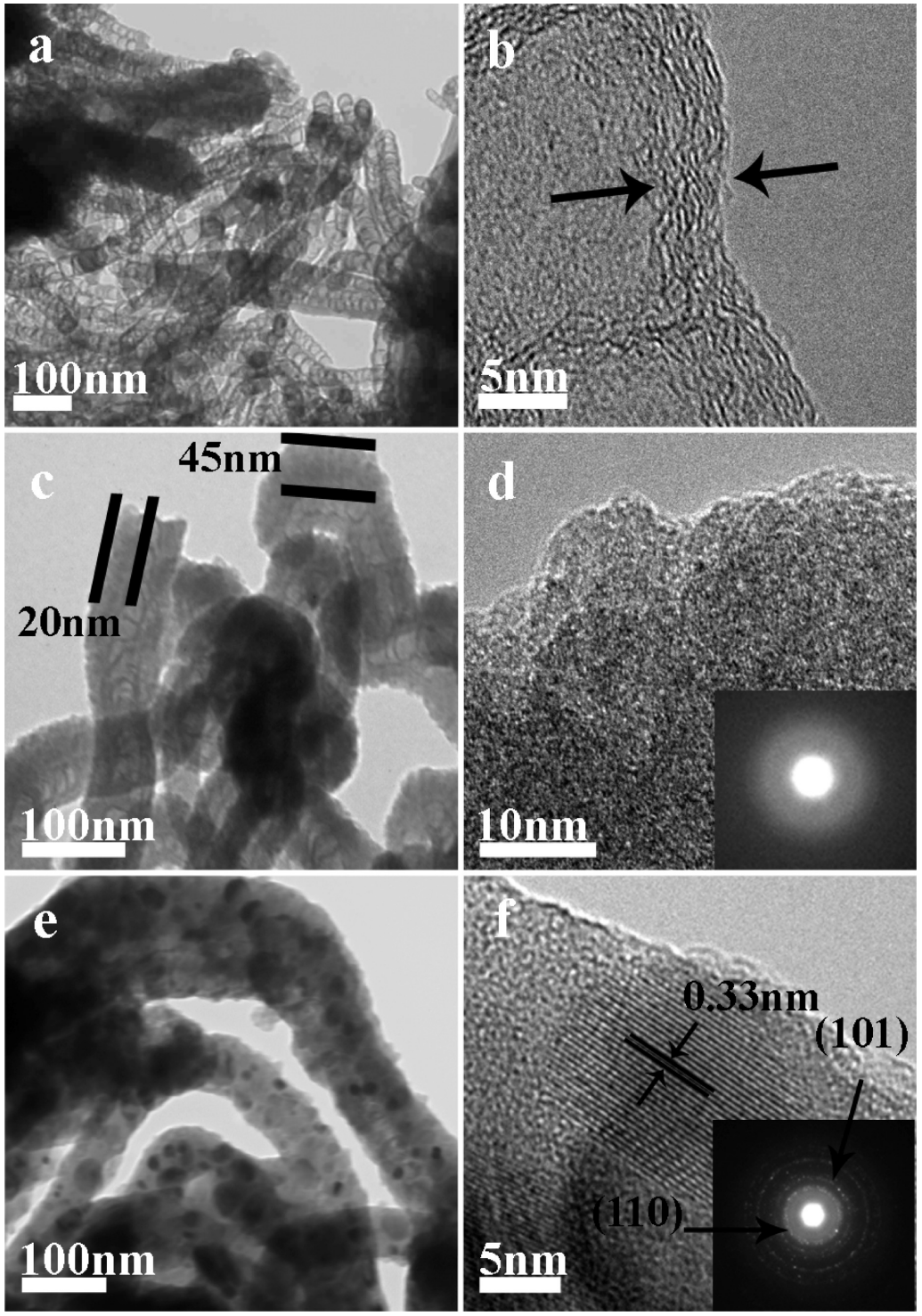

Figure 2. TEM and HRTEM images of composite nanostructures: (a, b) NCNTs; (c, d) $TiSi_2Ox$-NCNTs; (e, f) *An*-$TiSi_2O_x$-NCNTs.

open structure. However, it is evident in SEM images (Figure 1d) that there is an increase in the diameter of nanostructures, indicating the successful deposition of the $TiSi_2O_x$ layer on NCNTs. The thickness of the $TiSi_2O_x$ coating on NCNTs was controlled by sputtering power and time. The EDX analysis of these nanostructures (inset of Figure 1c) confirms the presence of Ti and Si with an approximate atomic ratio of 1:2. The oxygen was introduced into the deposited layer, as shown in the EDX spectrum through the residual oxygen in the chamber suggested in previous reports.[33−35] A closer observation of the composite nanostructures (Figure 1d) shows that the $TiSi_2O_x$ coating has particle-like morphology, which is common during sputtering on nanostructured materials at room temperature.[36,37]

To study the effect of the crystallinity of the coated layer, $TiSi_2O_x$-NCNTs were treated at high temperature (1000 °C) under an Ar environment and under a chamber pressure of 5 mbar. The morphology of the annealed $TiSi_2O_x$-NCNTs at 1000 °C for 6 h (*An*-$TiSi_2O_x$-NCNTs) is depicted in Figure 1e and f. The annealed nanostructures have a similar structure to

dx.doi.org/10.1021/jp3118874 | *J. Phys. Chem. C* 2013, 117, 15457−15467

pristine composite nanostructures but with smoother surfaces. In addition, as indicated in Figure 1f, in some areas, there is evidence of layer diffusion forming network structures. EDX analysis (inset of Figure 1f) of *An*-$TiSi_2O_x$-NCNTs indicates no significant change in the ratio of elements present in the coated layer. XRD analysis (Supporting Information, Figure S1) did not show any crystalline peaks corresponding to these nanostructures. This can be due to the small thickness of the sputtered layers of NCNTs.

TEM observations further reveal the unique morphology of these nanostructures. As shown in Figure 2a, the NCNTs have uniform diameters with nearly constant spaced bamboo-like structures. HRTEM images (Figure 2b) reveal that the NCNTs have a high degree of crystallinity in spite of the distorted nanotube walls, resulting from the regular joint defects, as explained by Liu et al.[24] Figure 2c shows the TEM image of $TiSi_2O_x$-NCNTs, revealing the nonuniform coverage of the $TiSi_2O_x$ layer on NCNTs. These observations indicate that the thickness of the $TiSi_2O_x$ coating on NCNTs varies from 0 to 60 nm due to the shielding effect of the sputtering technique. The thickness depends on the orientation of NCNTs with respect to the sputtering target. There have been similar studies on the formation of such nanostructures using sputtering on small and localized carbon nanotubes.[36−38] In these studies, sputtering was conducted on single or few carbon nanotubes, resulting in a better coverage of the coated area. The HRTEM image of $TiSi_2O_x$-NCNT composite nanostructures (Figure 2d) illustrates their amorphous nature. The SAED pattern shows diffused rings (inset of Figure 2d), further confirming their amorphous nature.[33]

Compared to $TiSi_2O_x$-NCNTs, the TEM images of *An*-$TiSi_2O_x$-NCNTs (Figure 2e) indicate the enhanced coverage of $TiSi_2O_x$ on NCNTs, confirming the diffusion of the coated layer under heat treatment. Furthermore, TEM images reveal the formation of nanoparticles in high density in the amorphous coating on NCNTs. HRTEM images of these nanoparticles shown in Figure 2f reveal that these nanoparticles are single crystalline with diameters between 5 and 10 nm and are partially covered by the amorphous layer. The lattice spacing of the nanoparticles is around 0.33 nm, corresponding to the {110} planes of rutile TiO_2. The SAED pattern (inset of Figure 3f) can be indexed as a tetragonal structure of rutile TiO_2. This is consistent with the results reported by Sankur et al.[39] and Goldstein et al.[40] Sankur et al.[39] reported the formation of rutile TiO_2 through annealing a cosputtered TiO_2−SiO_2 thin film at 1000 °C. They showed that the growth of TiO_2 crystalline particles in the amorphous matrix is diffusion-limited and decreases with decreasing TiO_2 content. There also have been several reports on the formation of various nanocrystals such as Si[41] and metal silicides[33,34,42,43] in an amorphous matrix. Since these types of reactions are a diffusion-controlled process, in order to obtain a higher degree of crystallinity, longer annealing time and higher temperature are required.

The chemical states of $TiSi_2O_x$ coating of the composite nanostructures were further studied using XAS. Figure 3a show the Si K edge (TEY) XANES of the $TiSi_2O_x$ samples. The XANES of a clean amorphous SiO_2 is also shown for comparison. According to Figure 3a, Si K edge XANES of both $TiSi_2O_x$-NCNTs and *An*-$TiSi_2O_x$-NCNTs exhibit features that are characteristic of SiO_2 at 1847 eV. In addition to the sharp SiO_2 resonance, the coated samples show a small feature at 1845 eV which is enhanced in $TiSi_2O_x$-NCNT samples

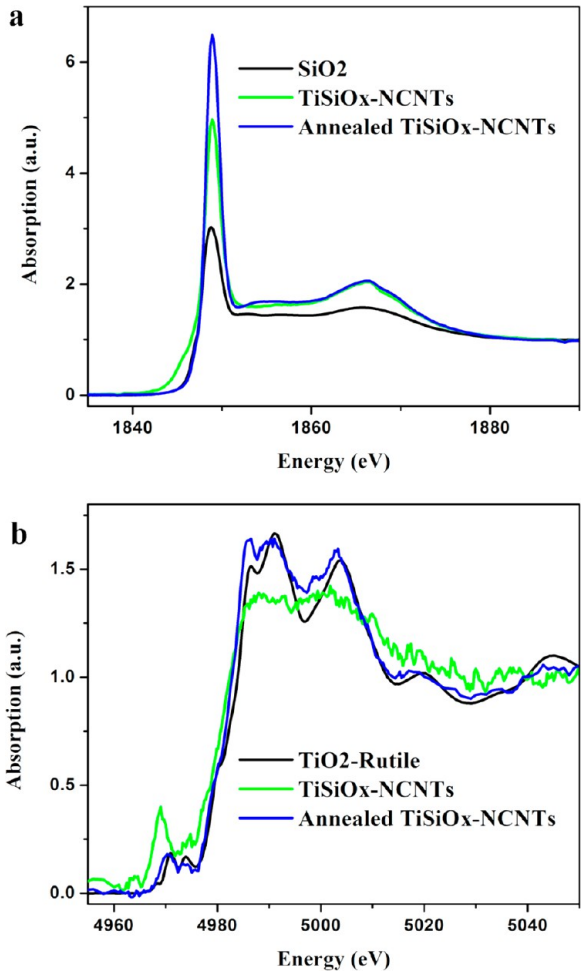

Figure 3. Normalized XANES spectra of composite catalyst supports at (a) the Si K edge and (b) the Ti K edge.

compared with annealed specimens. This feature is attributed to the 1s-σ^* resonance of the Si−O bond in the presence of silicon suboxides.[44] The reduction of the intensity of this feature in *An*-$TiSi_2O_x$-NCNT samples and the accompanying increase in the intensity of the 1847 peak is due to oxidation of the suboxides during the annealing process and formation of highly crystalline SiO_2 as judged by the sharpness of the resonance.

Figure 3b shows the Ti K edge XANES spectrum of the composite nanostructures and TiO_2 (rutile) powder as a reference sample. The characteristic feature of the Ti K edge spectra is the pre-edge weak features and the edge resonance arising from the excitation of a 1s electron into an empty bound state derived from the d and p states of Ti and O.[45,46] These pre-edge features probe the local symmetry of the Ti t_{2g} and E_g orbitals and their behavior upon local distortion.[47] The post edge features are mainly due to the multiple scattering contribution of the ejected photoelectron from higher shell neighboring atoms.[46] A number of studies have used the pre-edge intensity of the Ti K edge along with their positions to derive information from the Ti coordination chemistry, in compounds such as titanosilicate glass.[45,48,49] Shuji et al.[49] have reported that the pre-edge features of Ti K edge XANES provide the Ti coordination number based on the plot of peak energy versus peak high. They estimated the distortion using the intensity ratio between pre-edge peaks and Ti−Ti

dx.doi.org/10.1021/jp3118874 | J. Phys. Chem. C 2013, 117, 15457−15467

interaction strength from the rise and fall in peak intensity in the whole pre-edge region.

The XANES features of $TiSi_2O_x$-NCNTs shown in Figure 3b reveal a high intensity pre-edge peak with two small broad peaks on either side and a broad region with no distinct peaks in the multiple scattering region. The broad peak in the multiple scattering regions can be attributed to the absence of medium to long range order around the Ti atoms in the amorphous layer, confirming the HRTEM analysis of these samples. The distortion in the structure surrounding the Ti atoms in the short range, based on Shuji et al.[49] results, can further be confirmed by the features seen in the pre-edge region of $TiSi_2O_x$-NCNT samples, where the Ti is not in a well-defined symmetry environment.

However, the XANES features of *An*-$TiSi_2O_x$-NCNTs closely resemble those of the TiO_2 (rutile) and the pre-edge region of these composite structures has similar peak position and intensity, indicating the coordination chemistry of Ti in *A*-$TiSi_2O_x$-NCNTs is the same as rutile TiO_2 a D_{4h} local symmetry. This is also consistent with the HRTEM results of TiO_2 nanoparticle formation entailed by annealing. The small differences in the peak intensity in the pre-edge region and the multiple scattering area can be attributed to the size effect, as the same trend was reported by Wu et al. through comparing bulk and nanostructured TiO_2.[46] To further characterize the composite nanostructures and investigate the effect of $TiSi_2O_x$ coating and heat treatment on the structure of NCNTs, the nanostructures were characterized by means of Raman spectroscopy. Raman spectra of the three samples are plotted in Figure 4. In all of these three spectra, two prominent peaks at

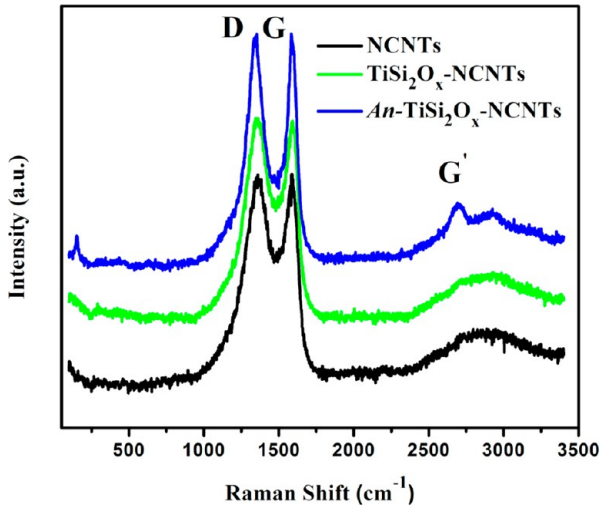

Figure 4. Raman spectrum of NCNTs and composite nanostructures deposited on carbon paper.

~1350 and ~1585 cm^{-1} known as the D band and G band, respectively, are observed. The I_D/I_G ratios of the three samples measured in Figure 4 indicate that there is no considerable change, accounting for around 0.9 in all three cases. This can be attributed to the relative lower annealing temperature (1000 °C) compared to the graphitization temperature of carbon (normally above 1500 °C).[50,51] However, the comparison of the fwhm of the D and G bands shows a considerable decrease in *An*-$TiSi_2$Ox-NCNT sample relative to NCNTs, indicating a change in the structure of composites. Furthermore, the Raman spectrum of *An*-$TiSi_2O_x$-NCNTs shows well distinct peaks in the range 2500−3000 cm^{-1}. The most prominent peak in this region corresponds to a second order Raman peak, G′, located at ~2700 cm^{-1}. Although the G′ band is independent of the structural defects, studies have shown that the intensity, shape, and position of this peak are sensitive to nitrogen incorporation in CNTs.[52] It has been reported that the intensity of the G′ band has an inverse relation with the nitrogen content of CNTs. In addition, previous studies have shown that, by annealing NCNTs at high temperatures (~1000 °C), the nitrogen content decreases dramatically due to release of trapped N_2 molecules and depletion of pyridine-like structures.[53] In this study, the appearance of the G′ band is an indicative change of the nitrogen content and the structure of NCNTs in annealed $TiSi_2O_x$-NCNTs. This reduction in nitrogen content, the changes in degree of disordered NCNTs, along with the formation of crystalline TiO_2 embedded in the SiO_2 amorphous layer collectively promote change in the surface chemistry of *An*-$TiSi_2O_x$-NCNTs compared to $TiSi_2O_x$-NCNTs.

Figure 5 shows TEM images of Pt nanoparticles deposited on the composite nanostructures synthesized on carbon paper. The TEM observation of the Pt/$TiSi_2O_x$-NCNTs samples (Figure 5a and b) indicates that Pt nanoparticles are mainly deposited on the bare surface of NCNT in contact with the $TiSi_2O_x$ coating. These Pt nanoparticles have a similar morphology to Pt deposited on NCNTs[28] with uniform diameters of 3 nm.

The nonuniformity of Pt nanoparticle dispersion on the composite can be attributed to the presence of SiO_x on the surface of $TiSi_2O_x$ coating. Studies have shown that Pt deposition on SiO_2 containing surfaces using conventional methods leads to limited uniformity and small Pt loading. This is because the Pt deposition using the reduction process requires a strong interaction between the Pt precursor and the substrate. When using H_2PtCl_6 as a Pt precursor in an acidic environment (even as low as pH 1), the ability of loading Pt onto the SiO_2 surface is reduced greatly, since there is no strong interaction between $PtCl_6^-$ and SiO_2 surfaces.

TEM images of Pt/*An*-$TiSi_2O_x$-NCNTs shown in Figure 5c reveal preferential deposition of Pt nanoparticles on the composite nanostructures which is similar to Pt/$TiSi_2O_x$-NCNTs. However, as shown in the HRTEM image of Pt/*An*-$TiSi_2O_x$-NCNTs, there are some Pt nanoparticles deposited on the *An*-$TiSi_2O_x$ layer, as shown in Figure 5d. These Pt nanoparticles are generally deposited on the nanocrystals formed on the surface coated layer. Furthermore, HRTEM images reveal, in contrast to the untreated composite samples, the Pt nanoparticles deposited on *An*-$TiSi_2O_x$-NCNTs are not spherical and have an aspect ratio of 1:2.5 with a small diameter of 3−4 nm. Sun et al.[23,54−56] have reported the synthesis of Pt nanorods and nanowires on various nanostructured supports by the reduction of Pt salt via formic acid in room temperature. Their studies showed the formation of nanorod-like Pt structures similar to those observed in Figure 5c and d. It is possible then, after annealing, the surface conditions of NCNTs promote the formation of rod-like Pt nanostructures under higher temperature within a short time.

To elucidate the effect of composite supports and the change in the morphology of Pt nanostructure on Pt chemical state and electronic structure, the XANES of Pt at the L_2 and L_3 edge were studied.

XANES at the Pt L_3 and L_2 edges for the Pt nanoparticles deposited on the composite structures are shown in Figure 6

dx.doi.org/10.1021/jp3118874 | J. Phys. Chem. C 2013, 117, 15457−15467

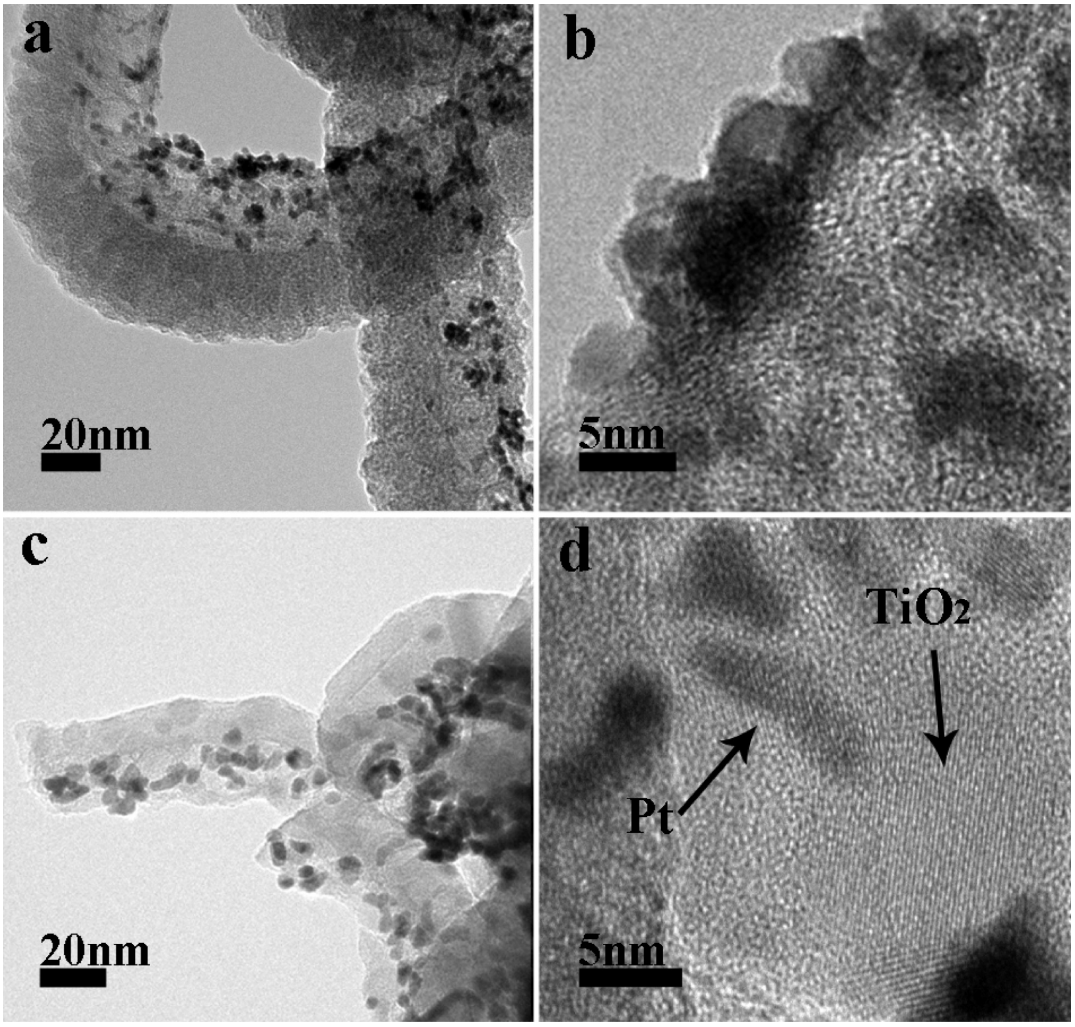

Figure 5. TEM images of Pt deposited nanostructures: (a, b) $TiSi_2O_x$-NCNT; (c, d) *An*-$TiSi_2O_x$-NCNT, grown on carbon paper.

including a Pt foil and Pt/NCNTs for comparison. It is seen that both Pt L_3 and L_2 edge XANES of supported Pt nanoparticles exhibit a considerable whiteline (WL) compared to the Pt foil. The WL in Pt L_2 and L_3 edges arises from the dominant $2p_{1/2}$ and $2p_{3/2}$ transition to $5d_{3/2}$ and $5d_{5/2,3/2}$, resectively (dipole selection rule: $\Delta l = \pm 1$, $\Delta j = \pm 1, 0$), indicating the presence of unoccupied densities of states of Pt $5d_{5/2}$ and $5d_{3/2}$ character in the samples.[57,58] The catalytic activity of Pt for various electrochemical reactions including ORR has been related to the density of states of employed Pt.[59,60] Furthermore, the interaction between the catalyst support and catalyst has been evaluated through study of the XANES spectrum.[19−21] The qualitative and quantitative interpretation of Pt L_2 and L_3 edge WL and XANES has been widely used to probe the unoccupied density of d states in a variety of systems.[57,58,61]

A close examination of the L_3 edge WL profile of the composite samples indicates that there are small differences in the L_3 edge WL intensity and shape. Results indicate that the L_3 edge WL intensity increases in the following order: Pt foil < Pt/NCNTs < Pt/$TiSi_2O_x$-NCNTs ∼ Pt/*An*-$TiSi_2O_x$-NCNTs. All composite samples show a positive shift in the maximum energy (E_{peak}) with small negative shift in the threshold energy (E_o, within experimental uncertainty). This indicates the Pt nanoparticles deposited on the composite supports are still metallic (a change in oxidation state to the common Pt(II), for example, still induces a significant shift). Thus, the increase in the WL intensity compared to Pt foil is due to decrease in the number of electrons in the d orbital, confirming a strong interaction between Pt nanoparticles and their support in the direction that Pt's d charge is depleted. The metallic behavior of these nanoparticles is also confirmed by the oscillations beyond the WL, which are characteristic of the fcc structure of Pt metal.

The corresponding L_2 edge WL (Figure 6b) shows a similar trend as that of the Pt L_3 edge in E_{peak} and E_o. However, as seen in the inset of Figure 6b, unlike the trend seen in the Pt L_3 edge, the L_2 WL intensity of Pt/$TiSi_2O_x$-NCNTs is slightly higher than that of Pt/*An*-$TiSi_2O_x$-NCNTs which may be due to the different chemical sensitivity of the $5d_{5/2}$ and $5d_{3/2}$ states in Pt d orbitals.[61]

For a better understanding of the effect of the unoccupied densities of 5d states of Pt nanoparticles on different supports, quantitative WL intensity analysis has been conducted on the basis of a method reported by Mansour et al.,[61] Sham et al.,[58] and Sun et al.[62] In this method, the Pt L_3 edge WL intensity is obtained by subtracting the Pt L_3 edge XANES from the corresponding XANES of Au. The area under the difference curve was integrated, and ΔA_3 and ΔA_2 were calculated. These values can be expressed as

dx.doi.org/10.1021/jp3118874 | J. Phys. Chem. C 2013, 117, 15457−15467

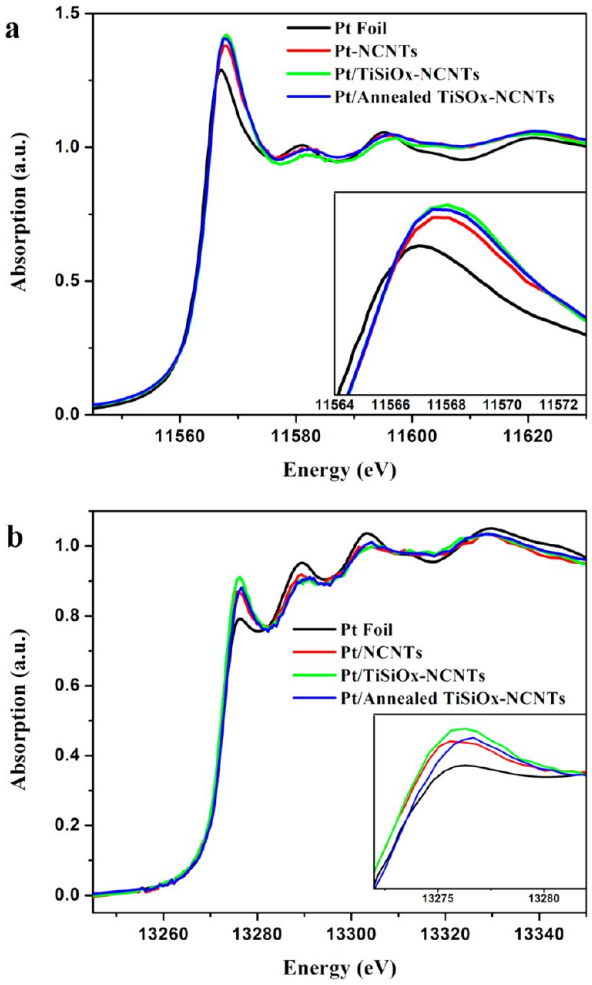

Figure 6. Normalized XANES spectra of Pt nanoparticles on composite catalyst support at (a) the Pt L_3 edge and (b) the Pt L_2 edge.

$$\Delta A_3 = \int \mu(\mathrm{Pt})_{L_3\mathrm{WL}} - \mu(\mathrm{Au})_{L_3\mathrm{WL}}$$

$$\Delta A_2 = \int \mu(\mathrm{Pt})_{L_2\mathrm{WL}} - \mu(\mathrm{Au})_{L_2\mathrm{WL}}$$

and according to Sham et al.,[58] the theoretical expressions of these value are

$$\Delta A_3 = C_o N_o E_3 (R_d^{2p_{3/2}})^2 \left[\frac{6h_{5/2} + h_{3/2}}{15}\right]$$

$$\Delta A_2 = C_o N_o E_2 (R_d^{2p_{1/2}})^2 \left(\frac{1}{3} h_{3/2}\right)$$

where $C_o = 4\pi r^2\alpha/3$ (α is the fine structure constant), N_0 is the density of Pt atoms, h_j are the 5d hole counts, and E_2 and E_3 are the corresponding edge thresholds, E_o, for the L_2 and L_3 edges, respectively. The R term is the radial transition matrix element. By assuming R terms are similar for both edges

$$C = C_o N_o R^2$$

and with this approximation

$$h_{5/2} = \frac{1}{2C}\left[5\frac{E_2}{E_3}\Delta A_3 - \Delta A_2\right]$$

$$h_{3/2} = \left[\frac{3\Delta A_2}{C}\right]$$

a C value of 7.484×10^4 cm^{-1} was derived for Pt metal by Matthesis et al.[63] Table 1 summarizes the Pt L_3 and Pt L_2 edge threshold and WL parameters. These results quantitatively confirm the observations made on the Pt L_3 edge XANES; i.e., Pt/*An*-$TiSi_2O_x$-NCNTs and Pt/$TiSi_2O_x$ have the highest total unoccupied density of states of Pt 5d character compared with Pt/NCNTs, indicating a higher SMSI between the composite supports and Pt catalysts. It can be concluded that this factor is one of the sources of the catalytic activity enhancement of Pt/*An*-$TiSi_2O_x$-NCNTs and Pt/$TiSi_2O_x$-NCNTs compared to Pt/NCNTs.

While XANES studies of Pt catalysts provide detailed information on the electronic structure and chemical environment of Pt nanostructures, they probe average properties and provide little information on the morphology and shape of the nanostructures.

Cyclic voltammetry (CV) measurements were carried out to study the electrochemical properties of Pt/$TiSi_2O_x$-NCNT and Pt/*An*-$TiSi_2O_x$-NCNT composites. For comparison, Pt/NCNT samples were examined under identical conditions. The CVs (Figure 7a) of these composite nanostructures were recorded in Ar-saturated 0.5 M H_2SO_4 aqueous solution at room temperature between −0.159 and 0.991 V vs Ag/AgCl (3 M NaCl), with a scan rate of 50 mVs^{-1}. The CV curves are normalized to the Pt loading of each sample. The Pt loading in Pt/*An*-$TiSi_2O_x$-NCNTs, Pt/$TiSi_2O_x$-NCNTs, and Pt/NCNTs was determined to be 0.12, 0.12, and 0.15 mg cm^{-2}, respectively. The voltammetric features of all the electrodes reveal the typical characteristics of Pt metal, with the adsorption and desorption of hydrogen between −0.154 and 0.1 V and Pt oxide formation and its reduction between 0.5 and 0.991 V. However, a closer observation on the reduction peak potential of Pt oxide of these three samples reveals that Pt/*An*-$TiSi_2O_x$-NCNTs show a positive shift compared with other samples. Previous studies demonstrated a correlation between the oxide reduction peak potential and the particle size.[64−66] Millared et al.[65,66] showed that the potential of the oxide reduction peak is strongly influenced by the particle size, with larger particles showing higher potentials. In addition, this shift in Pt oxide reduction peak is visible between Pt nanowires and Pt

Table 1. Pt L_3 Edge and Pt L_2 Edge Whiteline Parameters

	Pt L_3 edge WL				Pt L_2 edge WL					
sample	E_o (eV)	E_{Peak}(eV)	Γ (eV)	ΔA_3	E_o (eV)	E_{Peak} (eV)	Γ (eV)	ΔA_2	$h_{5/2}$	$h_{3/2}$
Pt foil	11564.00	11567.00	6.00	4.87	13273.00	13276.30	6.60	2.26	0.47	0.11
Pt/NCNTs	11563.98	11567.50	7.04	5.04	13272.98	13275.58	5.19	2.41	0.48	0.11
Pt/TiSiOx-NCNTs	11563.94	11568.06	8.23	5.10	13272.98	13276.38	6.81	3.15	0.49	0.15
Pt/*An*-TiSiOx-NCNTs	11563.98	11567.50	7.04	5.32	13273.00	13276.28	6.56	2.57	0.51	0.12

dx.doi.org/10.1021/jp3118874 | J. Phys. Chem. C 2013, 117, 15457−15467

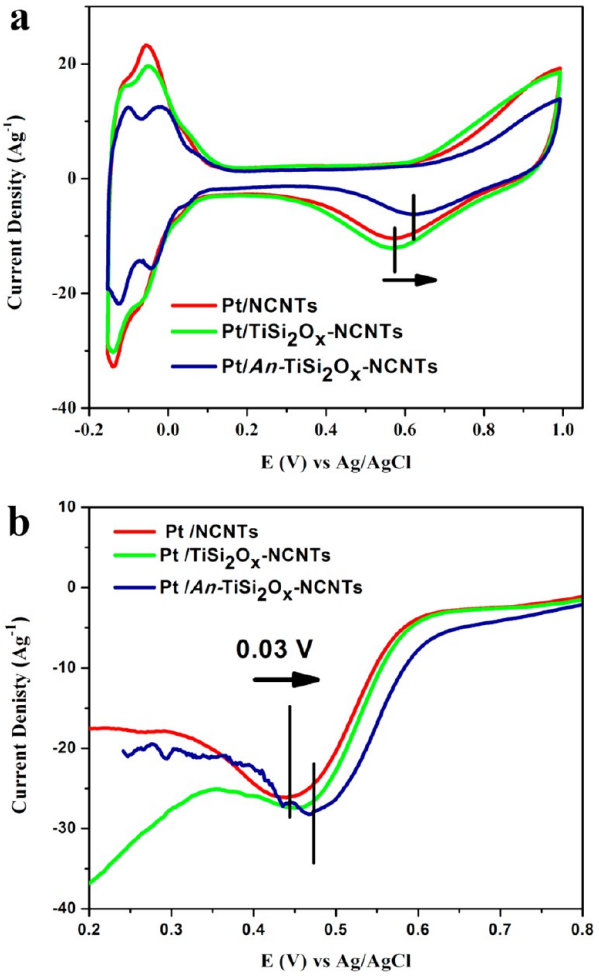

Figure 7. Electrochemical characterization of composite nanostructures: (a) cyclic voltammetry curves of Pt deposited composited nanostructures; (b) oxygen reduction curves of Pt deposited composite nanostructures. All samples were compared to Pt deposited nitrogen-doped carbon nanotubes.

nanoparticles with similar diameters.[23,54,56] Although the origin of this particle size effect still remains unclear, this shift observed in CV can be correlated to the difference in the morphology of Pt nanoparticles on the composite nanostructures observed in HRTEM images in Figure 5. Furthermore, the differences in features observed in the hydrogen adsorption and desorption region of CV curves of the electrocatalysts originates from the differences in the morphology of Pt nanostructures deposited on the supports. It is well-known that features in this region arise from hydrogen adsorption and desorption onto various Pt crystal planes. The presence of different ratios of Pt crystal planes results in different peak intensities in this region.[67]

The electrochemical surface area (ECSA) of the electrodes can be estimated from CV curves. The total charges of hydrogen desorption (Q_H) on the electrodes are calculated by integrating desorption peaks after excluding the double layer charging effect. Using the Q_H value and the Pt loading, it is possible to calculate the active Pt surface area (S_{EL}) according to the following formula:

$$S_{EL} = \frac{Q_H}{Q_{ref} \times Pt_{loading}}$$

S_{EL} is expressed in cm^2 mg^{-1}, where Pt loading is in mg$_{Pt}$ cm^{-2} and Q_{ref} = 0.21 mCcm^{-2}. This value corresponds to a surface density of 1.3 × 10^{15} atom cm^{-2} (a generally accepted value for a polycrystalline Pt electrode). Values of S_{EL} = 288.6 and 255.9 cm^2 mg^{-1} have been obtained for Pt nanoparticles deposited NCNTs, TiSi$_2$O$_x$-NCNTs, respectively, while S_{EL} = 179.6 cm^2 mg^{-1} has been calculated for Pt nanostructures deposited on *An*-TiSi$_2$O$_x$-NCNTs. This can be attributed to the intrinsic 1D morphology of Pt nanostructures compared to Pt nanoparticles deposited on composite nanostructures. This is in good agreement with previous results reported on Pt nanowires.[23,54,56]

The electrocatalytic activities for ORR of the composite electrodes are compared in Figure 4b by linear scanning voltammetry at a scan rate of 50 mVs^{-1}. Pt/*An*-TiSi$_2$O$_x$-NCNTs show a higher peak potential than the other two electrodes. The peak potential of Pt/*An*-TiSi$_2$O$_x$-NCNTs is 0.47 V, while those of Pt/NCNTs and Pt/TiSi$_2$O$_x$-NCNTs are both at 0.44 V, suggesting that Pt/*An*-TiSi$_2$O$_x$ exhibits a 30 mV positive shift of the peak potential compared to the latter two electrodes toward ORR. At peak potential, the mass activity on Pt/*An*-TiSi$_2$O$_x$-NCNTs (28.3 Ag^{-1}) is about 1.1 times higher than that on Pt/NCNTs (26.1 Ag^{-1}) and 1.02 times higher than that on Pt/TiSi$_2$O$_x$-NCNTs (27.7 Ag^{-1}). This improvement occurred in spite of a 50% lower Pt active surface area for the Pt/*An*-TiSi$_2$O$_x$-NCNTs compared to Pt/NCNTs. By taking into account the active surface area, the specific ORR activity for Pt/*An*-TiSi$_2$O$_x$-NCNTs (1.54 Am^{-2}) is 1.7 times larger than that for Pt/NCNTs (0.9 Am^{-2}) and 1.4 times larger than that for Pt/TiSi$_2$O$_x$-NCNTs (1.08 Am^{-2}). The large specific activity and mass activity and more positive peak potential indicate that Pt/*An*-TiSi$_2$O$_x$-NCNTs has a higher intrinsic electrocatalytic activity than Pt/TiSi$_2$O$_x$-NCNTs, which itself is higher than Pt/NCNTs.

CONCLUSION

In summary, composite nanostructures of NCNTs coated with TiSi$_2$O$_x$ were synthesized as Pt catalyst supports for ORR. The nanostructures were synthesized using a combination of CVD and magnetron sputtering processes. Experimental results showed that TiSi$_2$O$_x$ formed an amorphous layer with variable thickness on CNTs. Annealing treatment of the composite nanostructures promoted the formation of TiO$_2$ nanocrystals embedded in the amorphous TiSi$_2$O$_x$ matrix. XANES spectra of Ti K edge and Si K edge confirmed the presence of rutile TiO$_2$ and SiO$_2$ in the sputtered layer. Electrochemical properties of Pt deposited composite nanostructure were investigated. Compared to Pt/TiSi$_2$O$_x$-NCNTs and Pt/NCNTs, Pt/*An*-TiSi$_2$O$_x$-NCNTs exhibited a 30 mV positive potential and higher mass and specific activity for ORR. XANES spectra of Pt L$_2$ edge and Pt L$_3$ edge and their quantitative whiteline analysis of the three electrocatalysts confirmed the presence of a higher density of unoccupied states in Pt 5d orbitals for Pt on composite supports compared with NCNTs. These results indicate a SMSI between composite supports and Pt, which leads to higher catalytic activity. TEM observations reveal the formation of Pt nanorod-like structures on *An*-TiSi$_2$O$_x$-NCNTs compared to sphere-like nanoparticles deposited on pristine TiSi$_2$O$_x$-NCNTs. The higher performance of Pt/*An*-TiSi$_2$O$_x$-NCNTs than Pt/TiSi$_2$O$_x$-NCNTs is attributed to the nanorod-like shape of Pt and the synergistic effect between Pt, SiO$_x$, and TiO$_2$ on the annealed TiSi$_2$O$_x$ layer (Pt 5d charge depletion). Our results show that multicomponent composite nanostruc-

dx.doi.org/10.1021/jp3118874 | J. Phys. Chem. C 2013, 117, 15457−15467

tures are promising supports for oxygen reduction reactions in PEMFCs.

■ ASSOCIATED CONTENT

Supporting Information

Figure showing the XRD patterns of $TiSi_2O_x$-NCNTs and *An*-$TiSi_2O_x$-NCNTs. This material is available free of charge via the Internet at http://pubs.acs.org.

■ AUTHOR INFORMATION

Corresponding Author

*E-mail: xsun@eng.uwo.ca. Phone: +1 (519) 661-2111, ext. 87759.

Notes

The authors declare no competing financial interest.

■ ACKNOWLEDGMENTS

This research was supported by General Motors of Canada, Natural Sciences and Engineering Research Council of Canada, Ontario Centres of Excellence, Canada Research Chair Program, Canada Foundation for Innovation, and the University of Western Ontario.

■ REFERENCES

(1) Andress, D.; Das, S.; Joseck, F.; Dean Nguyen, T. Status of Advanced Light Duty Transportation Technologies in the US. *Energy Policy* **2012**, *41*, 348−364.

(2) Higgins, D. C.; Meza, D.; Chen, Z. Nitrogen Doped Carbon Nanotubes as Platinum Catalyst Supports for Oxygen Reduction Reaction in Proton Exchange Membrane Fuel Cells. *J. Phys. Chem. C* **2010**, *114*, 21982−21988.

(3) Saha, M. S.; Li, R.; Sun, X.; Ye, S. 3-D Composite Electrodes for High Performance PEM Fuel Cells Composed of Pt Supported on Nitrogen-Doped Carbon Nanotubes Grown on Carbon Paper. *Electrochem. Commun.* **2009**, *11*, 438−441.

(4) Chen, Y.; Wang, J.; Liu, H.; Li, R.; Sun, X.; Ye, S.; Knights, S. Enhanced Stability of Pt Electrocatalysts by Nitrogen Doping in CNTs for PEM Fuel Cells. *Electrochem. Commun.* **2009**, *11*, 2071−2076.

(5) Xiong, W.; Du, F.; Liu, Y.; Perez, A.; Supp, M.; Ramakrishnan, T. S.; Dai, L.; Jiang, L. 3-D Carbon Nanotube Structures Used as High Performance Catalyst for Oxygen Reduction Reaction. *J. Am. Chem. Soc.* **2010**, *132*, 15839−15841.

(6) Chen, Z.; Higgins, D.; Tao, H.; Hsu, R. S.; Chen, Z. Highly Active Nitrogen Doped Carbon Nanotubes for Oxygen Reduction Reaction in Fuel Cell Applications. *J. Phys. Chem. C* **2009**, *113*, 21008−21013.

(7) Gong, K.; Du, F.; Xia, Z.; Durstock, M.; Dai, L. Nitrogen-Doped Carbon Nanotube Arrays with High Electrocatalytic Activity for Oxygen Reduction. *Science* **2009**, *323*, 760−764.

(8) Sun, X.; Li, R.; Villers, D.; Dodelet, J. P.; Désilets, S. Composite Electrodes Made of Pt Nanoparticles Deposited on Carbon Nanotubes Grown on Fuel Cell Backings. *Chem. Phys. Lett.* **2003**, *379*, 99−104.

(9) Saha, M. S.; Li, R.; Sun, X. High Loading and Monodispersed Pt Nanoparticles on Multiwalled Carbon Nanotubes for High Performance Proton Exchange Membrane Fuel Cells. *J. Power Sources* **2008**, *177*, 314−322.

(10) Sun, X.; Li, R.; Stansfield, B.; Dodelet, J. P.; Désilets, S. 3D Carbon Nanotube Network Based on a Hierarchical Structure Grown on Carbon Paper Backing. *Chem. Phys. Lett.* **2004**, *394*, 266−270.

(11) Saha, M. S.; Banis, M. N.; Zhang, Y.; Li, R.; Sun, X.; Cai, M.; Wagner, F. T. Tungsten Oxide Nanowires Grown on Carbon Paper as Pt Electrocatalyst Support for High Performance Proton Exchange Membrane Fuel Cells. *J. Power Sources* **2009**, *192*, 330−335.

(12) Saha, M. S.; Li, R.; Cai, M.; Sun, X. High Electrocatalytic Activity of Platinum Nanoparticles on SnO_2 Nanowire-Based Electrodes. *Electrochem. Solid-State Lett.* **2007**, *10*, B130−B133.

(13) Jeon, M. K.; Daimon, H.; Lee, K. R.; Nakahara, A.; Woo, S. I. CO Tolerant Pt/WC Methanol Electro-Oxidation Catalyst. *Electrochem. Commun.* **2007**, *9*, 2692−2695.

(14) Antolini, E.; Gonzalez, E. R. Ceramic Materials as Supports for Low-Temperature Fuel Cell Catalysts. *Solid State Ionics* **2009**, *180*, 746−763.

(15) Antolini, E. Composite Materials: An Emerging Class of Fuel Cell Catalyst Supports. *Appl. Catal., B* **2010**, *100*, 413−426.

(16) Kang, S. H.; Sung, Y.-E.; Smyrl, W. H. The Effectiveness of Sputtered PtCo Catalysts on TiO_2 Nanotube Arrays for the Oxygen Reduction Reaction. *J. Electrochem. Soc.* **2008**, *155*, B1128−B1135.

(17) Beak, S.; Jung, D.; Nahm, K. S.; Kim, P. Preparation of Highly Dispersed Pt on TiO_2-Modified Carbon for the Application to Oxygen Reduction Reaction. *Catal. Lett.* **2010**, *134*, 288−294.

(18) Wang, R.; Li, X.; Wang, Q.; Wang, H.; Wang, W.; Kang, J.; Chang, Y.; Lei, Z. Highly Stable and Effective Pt/carbon Nitride (CNx) Modified SiO_2 Electrocatalyst for Oxygen Reduction Reaction. *Int. J. Hydrogen Energy* **2011**, *36*, 5775−5781.

(19) Zhou, J.; Zhou, X.; Sun, X.; Murphy, M.; Ding, Z.; Sun, X.; Sham, T. K. Interaction Between Pt Nanoparticles and Carbon Nanotubes - An X-ray Absorption Near Edge Structures (XANES) Study. *Chem. Phys. Lett.* **2007**, *437*, 229−232.

(20) Jia, J.; Kou, Y.; Lin, L.; Xu, Z.; Zhang, T.; Niu, J.; Liang, D. Pt L_{III}-Edge XANES and EXAFS Studies on γ-Al_2O_3 Supported Pt Catalysts. *React. Kinet. Catal. Lett.* **1998**, *63*, 391−396.

(21) Boyanov, B. I.; Morrison, T. I. Support and Temperature Effects in Platinum Clusters. 2. Electronic Properties. *J. Phys. Chem.* **1996**, *100*, 16318−16326.

(22) Mazumder, V.; Lee, Y.; Sun, S. Recent Development of Active Nanoparticle Catalysts for Fuel Cell Reactions. *Adv. Funct. Mater.* **2010**, *20*, 1224−1231.

(23) Sun, S.; Jaouen, F.; Dodelet, J. Controlled Growth of Pt Nanowires on Carbon Nanospheres and Their Enhanced Performance as Electrocatalysts in PEM Fuel Cells. *Adv. Mater.* **2008**, *20*, 3900−3904.

(24) Liu, H.; Zhang, Y.; Li, R.; Sun, X.; Désilets, S.; Abou-Rachid, H.; Jaidann, M.; Lussier, L.-S. Structural and Morphological Control of Aligned Nitrogen-Doped Carbon Nanotubes. *Carbon* **2010**, *48*, 1498−1507.

(25) Meng, X.; Zhong, Y.; Sun, Y.; Banis, M. N.; Li, R.; Sun, X. Nitrogen-Doped Carbon Nanotubes Coated by Atomic Layer Deposited SnO2 with Controlled Morphology and Phase. *Carbon* **2011**, *49*, 1133−1144.

(26) Chen, Y.; Wang, J.; Liu, H.; Banis, M. N.; Li, R.; Sun, X.; Sham, T.-K.; Ye, S.; Knights, S. Nitrogen Doping Effects on Carbon Nanotubes and the Origin of the Enhanced Electrocatalytic Activity of Supported Pt for Proton-Exchange Membrane Fuel Cells. *J. Phys. Chem. C* **2011**, *115*, 3769−3776.

(27) Hu, Y. F.; Coulthard, I.; Chevrier, D.; Wright, G.; Igarashi, R.; Sitnikov, A.; Yates, B. W.; Hallin, E. L.; Sham, T. K.; Reininger, R. Preliminary Commissioning and Performance of the Soft X-ray Micro-Characterization Beamline at the Canadian Light Source. *AIP Conf. Proc.* **2010**, *1234*, 343−346.

(28) Yang, D.-Q.; Sun, S.; Dodelet, J.-P.; Sacher, E. A Facile Route for the Self-Organized High-Density Decoration of Pt Nanoparticles on Carbon Nanotubes. *J. Phys. Chem. C* **2008**, *112*, 11717−11721.

(29) Sun, S. H.; Yang, D. Q.; Villers, D.; Zhang, G. X.; Sacher, E.; Dodelet, J. P. Template- and Surfactant-Free Room Temperature Synthesis of Self-Assembled 3D Pt Nanoflowers from Single-Crystal Nanowires. *Adv. Mater.* **2008**, *20*, 571−574.

(30) Cheung, C. L.; Kurtz, A.; Park, H.; Lieber, C. M. Diameter-Controlled Synthesis of Carbon Nanotubes. *J. Phys. Chem. B* **2002**, *106*, 2429−2433.

(31) Wang, X.; Liu, Y.; Zhu, D.; Zhang, L.; Ma, H.; Yao, N.; Zhang, B. Controllable Growth, Structure, and Low Field Emission of Well-Aligned CNx Nanotubes. *J. Phys. Chem. B* **2002**, *106*, 2186−2190.

(32) He, M.; Zhou, S.; Zhang, J.; Liu, Z.; Robinson, C. CVD Growth of N-Doped Carbon Nanotubes on Silicon Substrates and Its Mechanism. *J. Phys. Chem. B* **2005**, *109*, 9275−9279.

(33) Broadbent, E. K.; Morgan, A. E.; Coulman, B.; Huang, I. -W. Characterization of Titanium Silicide Films Formed by Composite Sputtering and Rapid Thermal Annealing. *Thin Solid Films* **1987**, *151*, 51−63.
(34) Pantel, R.; Levy, D.; Nicolas, D.; Ponpon, J. P. Oxygen Behavior during Titanium Silicide Formation by Rapid Thermal Annealing. *J. Appl. Phys.* **1987**, *62*, 4319−4321.
(35) Wee, A. T. S.; Huan, A. C. H.; Osipowicz, T.; Lee, K. K.; Thian, W. H.; Tan, K. L.; Hogan, R. Surface and Interface Studies of Titanium Silicide Formation. *Thin Solid Films* **1996**, *283*, 130−134.
(36) Nam, C.; Kim, Y.-S.; Kim, W. B.; Cho, B. K. Magnetic Dipolar Interaction in NiFe Nanodot Arrays Formed on Vertical Carbon Nanotubes. *Nanotechnology* **2008**, *19*, 475703−475707.
(37) Wilson, N. R.; Macpherson, J. V. Single-Walled Carbon Nanotubes as Templates for Nanowire Conducting Probes. *Nano Lett.* **2003**, *3*, 1365−1369.
(38) Rogachev, A.; Bezryadin, A. Superconducting Properties of Polycrystalline Nb Nanowires Templated by Carbon Nanotubes. *Appl. Phys. Lett.* **2003**, *83*, 512−515.
(39) Sankur, H.; Gunning, W. Crystallization and Diffusion in Composite TiO_2-SiO_2 Thin Films. *J. Appl. Phys.* **1989**, *66*, 4747−4751.
(40) Goldstein, J. I.; Choi, S. K.; Van Loo, F. J. J.; Bastin, G. F.; Metselaar, R. Solid-State Reactions and Phase Relations in the Ti-Si-O System at 1373 K. *J. Am. Ceram. Soc.* **1995**, *78*, 313−322.
(41) Gencer Imer, A.; Yildiz, I.; Turan, R. Fabrication of Si Nanocrystals in an Amorphous SiC Matrix by Magnetron Sputtering. *Physica E* **2010**, *42*, 2358−2363.
(42) Sadoh, T.; Owatari, M.; Murakami, Y.; Kenjo, A.; Yoshitake, T.; Itakura, M.; Enokida, T.; Miyao, M. Formation of SiGe/[beta]-$FeSi_2$ Superstructures from Amorphous Si/FeSiGe Layers. *Thin Solid Films* **2004**, *461*, 77−80.
(43) Hofman, D.; Kleint, C.; Thomas, J.; Wetzig, K. Investigation of Thermoelectric Silicide Thin Films by Means of Analytical Transmission Electron Microscopy. *Ultramicroscopy* **2000**, *81*, 271−277.
(44) Sammynaiken, R.; Naftel, S. J.; Sham, T. K.; Cheah, K. W.; Averboukh, B.; Huber, R.; Shen, Y. R.; Qin, G. G.; Ma, Z. C.; Zong, W. H. Structure and Electronic Properties of SiO_2/Si Multilayer Superlattices: Si K Edge and $L_{3,2}$ Edge X-ray Absorption Fine Structure Study. *J. Appl. Phys.* **2002**, *92*, 3000−3006.
(45) Lee, J. S.; Kim, W. B.; Choi, S. H. Linear Combination of XANES for Quantitative Analysis of Ti−Si Binary Oxides. *J. Synchrotron Radiat.* **2001**, *8*, 163−167.
(46) Wu, Z. Y.; Zhang, J.; Ibrahim, K.; Xian, D. C.; Li, G.; Tao, Y.; Hu, T. D.; Bellucci, S.; Marcelli, A.; Zhang, Q. H.; Gao, L.; Chen, Z. Z. Structural Determination of Titanium-Oxide Nanoparticles by X-ray Absorption Spectroscopy. *Appl. Phys. Lett.* **2002**, *80*, 2973−2975.
(47) Yogi, C.; Kojima, K.; Hashishin, T.; Wada, N.; Inada, Y.; Della Gaspera, E.; Bersani, M.; Martucci, A.; Liu, L.; Sham, T.-K. Size Effect of Au Nanoparticles on TiO_2 Crystalline Phase of Nanocomposite Thin Films and Their Photocatalytic Properties. *J. Phys. Chem. C* **2011**, *115*, 6554−6560.
(48) Farges, F.; Brown, G. E.; Rehr, J. J. Ti K-edge XANES Studies of Ti Coordination and Disorder in Oxide Compounds: Comparison between Theory and Experiment. *Phys. Rev. B* **1997**, *56*, 1809−1819.
(49) Shuji, M.; Nahomi, S.; Hisanobu, W. Pre-Edge Features of Ti K-Edge X-Ray Absorption Near-Edge Structure for the Local Structure of Sol-Gel Titanium Oxides. *Anal. Sci.* **2005**, *21*, 805−809.
(50) Gong, Q. M.; Li, Z.; Wang, Y.; Wu, B.; Zhang, Z.; Liang, J. The Effect of High-Temperature Annealing on the Structure and Electrical Properties of Well-Aligned Carbon Nanotubes. *Mater. Res. Bull.* **2007**, *42*, 474−481.
(51) Chen, J.; Shan, J. Y.; Tsukada, T.; Munekane, F.; Kuno, A.; Matsuo, M.; Hayashi, T.; Kim, Y. A.; Endo, M. The Structural Evolution of Thin Multi-Walled Carbon Nanotubes during Isothermal Annealing. *Carbon* **2007**, *45*, 274−280.
(52) Bulusheva, L. G.; Okotrub, A. V.; Kinloch, I. A.; Asanov, I. P.; Kurenya, A. G.; Kudashov, A. G.; Chen, X.; Song, H. Effect of Nitrogen Doping on Raman Spectra of Multi-Walled Carbon Nanotubes. *Phys. Status Solidi B* **2008**, *245*, 1971−1974.
(53) Choi, H. C.; Bae, S. Y.; Jang, W.-S.; Park, J.; Song, H. J.; Shin, H.-J.; Jung, H.; Ahn, J.-P. Release of N_2 from the Carbon Nanotubes via High-Temperature Annealing. *J. Phys. Chem. B* **2005**, *109*, 1683−1688.
(54) Sun, S.; Zhang, G.; Geng, D.; Chen, Y.; Banis, M. N.; Li, R.; Cai, M.; Sun, X. Direct Growth of Single-Crystal Pt Nanowires on Sn@CNT Nanocable: 3D Electrodes for Highly Active Electrocatalysts. *Chem.—Eur. J.* **2010**, *16*, 829−835.
(55) Sun, S.; Yang, D.; Zhang, G.; Sacher, E.; Dodelet, J.-P. Synthesis and Characterization of Platinum Nanowire−Carbon Nanotube Heterostructures. *Chem. Mater.* **2007**, *19*, 6376−6378.
(56) Sun, S.; Zhang, G.; Geng, D.; Chen, Y.; Li, R.; Cai, M.; Sun, X. A Highly Durable Platinum Nanocatalyst for Proton Exchange Membrane Fuel Cells: Multiarmed Starlike Nanowire Single Crystal. *Angew. Chem., Int. Ed.* **2011**, *50*, 422−426.
(57) Brown, M.; Peierls, R. E.; Stern, E. A. White Lines in X-ray Absorption. *Phys. Rev. B: Solid State* **1977**, *15*, 738−744.
(58) Sham, T. K.; Naftel, S. J.; Coulthard, I. $M_{3,2}$-Edge X-ray Absorption Near-Edge Structure Spectroscopy: An Alternative Probe to the $L_{3,2}$-Edge Near-Edge Structure for the Unoccupied Densities of d States of 5d Metals. *J. Appl. Phys.* **1996**, *79*, 7134−7138.
(59) Min, M.-K.; Cho, J.; Cho, K.; Kim, H. Particle Size and Alloying Effects of Pt-Based Alloy Catalysts for Fuel Cell Applications. *Electrochim. Acta* **2000**, *45*, 4211−4217.
(60) Lima, F.; Zhang, J.; Shao, M.; Sasaki, K.; Vukmirovic, M.; Ticianelli, E.; Adzic, R. Pt Monolayer Electrocatalysts for O_2 Reduction: PdCo/C Substrate-Induced Activity in Alkaline Media. *J. Solid State Electrochem.* **2008**, *12*, 399−407.
(61) Mansour, A. N.; Cook, J. W.; Sayers, D. E. Quantitative Technique for the Determination of the Number of Unoccupied D-Electron States in a Platinum Catalyst Using the $L_{2,3}$ X-ray Absorption Edge Spectra. *J. Phys. Chem.* **1984**, *88*, 2330−2334.
(62) Sun, S.; Zhang, G.; Gauquelin, N.; Chen, N.; Zhou, J.; Yang, S.; Chen, W.; Meng, X.; Geng, D.; Banis, M. N.; Li, R.; Ye, S.; Knights, S.; Botton, G. A.; Sham, T.-K.; Sun, X. Single-Atom Catalysis Using Pt/Graphene Achieved through Atomic Layer Deposition. *Sci. Rep.* **2013**, *3*, 1−9.
(63) Mattheiss, L. F.; Dietz, R. E. Relativistic Tight-Binding Calculation of Core-Valence Transitions in Pt and Au. *Phys. Rev. B* **1980**, *22*, 1663−1676.
(64) Ciapina, E. G.; Santos, S. F.; Gonzalez, E. R. The Electrooxidation of Carbon Monoxide on Unsupported Pt Agglomerates. *J. Electroanal. Chem.* **2010**, *644*, 132−143.
(65) Maillard, F.; Schreier, S.; Hanzlik, M.; Savinova, E. R.; Weinkauf, S.; Stimming, U. Influence of Particle Agglomeration on the Catalytic Activity of Carbon-Supported Pt Nanoparticles in CO Monolayer Oxidation. *Phys. Chem. Chem. Phys.* **2005**, *7*, 385−393.
(66) Maillard, F.; Eikerling, M.; Cherstiouk, O. V.; Schreier, S.; Savinova, E.; Stimming, U. Size Effects on Reactivity of Pt Nanoparticles in CO Monolayer Oxidation: The Role of Surface Mobility. *Faraday Discuss.* **2004**, *125*, 357−377.
(67) Kita, H.; Ye, S.; Aramata, A.; Furuya, N. Adsorption of Hydrogen on Platinum Single Crystal Electrodes in Acid and Alkali Solutions. *J. Electroanal. Chem. Interfacial Electrochem.* **1990**, *295*, 317−331.